Supplementary Information: Experimental evidence for Zeeman spin-orbit coupling in layered antiferromagnetic conductors

R. Ramazashvili,[1,*] P. D. Grigoriev,[2,3,4] T. Helm,[5,6,7,†] F. Kollmannsberger,[5,6] M. Kunz,[5,6,‡] W. Biberacher,[5] E. Kampert,[7] H. Fujiwara,[8] A. Erb,[5,6] J. Wosnitza,[7,9] R. Gross,[5,6,10] and M. V. Kartsovnik[5,§]

[1]*Laboratoire de Physique Théorique, Université de Toulouse, CNRS, UPS, France*
[2]*L. D. Landau Institute for Theoretical Physics, 142432 Chernogolovka, Russia*
[3]*National University of Science and Technology MISiS, 119049 Moscow, Russia*
[4]*P.N. Lebedev Physical Institute, 119991 Moscow, Russia*
[5]*Walther-Meißner-Institut, Bayerische Akademie der Wissenschaften, Walther-Meißner-Strasse 8, D-85748 Garching, Germany*
[6]*Physik-Department, Technische Universität München, D-85748 Garching, Germany*
[7]*Hochfeld-Magnetlabor Dresden (HLD-EMFL) and Würzburg-Dresden Cluster of Excellence ct.qmat, Helmholtz-Zentrum Dresden-Rossendorf, 01328 Dresden, Germany*
[8]*Department of Chemistry, Graduate School of Science, Osaka Prefecture University, Osaka 599-8531, Japan*
[9]*Institut für Festkörper- und Materialphysik, TU Dresden, 01062 Dresden, Germany*
[10]*Munich Center for Quantum Science and Technology (MCQST), D-80799 Munich, Germany*

(Dated: December 23, 2020)

SUPLEMENTARY NOTE I. SPIN-REDUCTION FACTOR $R_s(\theta)$ IN A MAGNETIC FIELD PERPENDICULAR TO THE NÉEL AXIS

For a quasi-2D metal, the phase φ of the first quantum-oscillation harmonic (i.e., of the fundamental frequency oscillations) is, up to a constant, $\varphi = \frac{F}{B} = \frac{\hbar}{e}\frac{\mathcal{F}}{B\cos\theta}$, where θ is the tilt angle between the field and the normal to the conducting plane, F stands for the oscillation frequency at $\theta = 0°$, and $\mathcal{F}$ the corresponding Fermi-surface area. The Zeeman effect splits the spin-degenerate Fermi surface, breaking up $\mathcal{F}$ into $\mathcal{F}_+$ and $\mathcal{F}_-$, with $\delta\mathcal{F} = \mathcal{F}_+ - \mathcal{F}_- \propto B$. Adding the two harmonic oscillations at close frequencies F_+ and F_- is equivalent to a single oscillation at frequency F, with an amplitude modulated by the spin-reduction factor

$$R_s(\theta) = \cos\left[\frac{\hbar}{2e}\frac{\delta\mathcal{F}}{B\cos\theta}\right]. \tag{1}$$

For the field perpendicular to the Néel axis, $\mathbf{B} = \mathbf{B}_\perp$, Eq. (1) of the main text yields the single-particle Hamiltonian: $\mathcal{H} = \mathcal{E}(\mathbf{k}) - \frac{1}{2}\mu_B g_\perp(\mathbf{k})(\mathbf{B}_\perp\cdot\boldsymbol{\sigma})$, where $\mathcal{E}(\mathbf{k})$ is the zero-field dispersion near the Fermi surface, and $\boldsymbol{\sigma} = (\sigma^x, \sigma^y, \sigma^z)$ is a vector composed of the three Pauli matrices. Upon turning on the field, a given point $\mathbf{k}$ of the Fermi surface undergoes a small shift $\delta\mathbf{k}$ such that $\delta\mathbf{k}\cdot\boldsymbol{\nabla}_\mathbf{k}\mathcal{E}(\mathbf{k}) = \pm\frac{1}{2}\mu_B g_\perp(\mathbf{k})B_\perp$, where the $\pm$ signs correspond to the 'up' and 'down' spin projections on $\mathbf{B}_\perp$ and to the subscript of the resulting Fermi-surface areas $\mathcal{F}_\pm$. As shown in Fig. 1, upon the shift by $\delta\mathbf{k}$ an element dk of the Fermi surface contributes the shaded area $dk(\delta\mathbf{k}\cdot\hat{\mathbf{l}}_\mathbf{k}) = \pm\frac{1}{2}\mu_B B_\perp dk g_\perp(\mathbf{k})/|\boldsymbol{\nabla}_\mathbf{k}\mathcal{E}(\mathbf{k})|$ to the variation of the total area, enclosed by the Fermi surface. Here, $\hat{\mathbf{l}}_\mathbf{k} = \boldsymbol{\nabla}_\mathbf{k}\mathcal{E}(\mathbf{k})/|\boldsymbol{\nabla}_\mathbf{k}\mathcal{E}(\mathbf{k})|$ is the local unit vector, normal to the Fermi surface. Therefore, to linear order in $B_\perp$, the areas $\mathcal{F}_\pm$ of the two spin-split Fermi surfaces differ by

$$\delta\mathcal{F} = \mathcal{F}_+ - \mathcal{F}_- = \mu_B B_\perp \oint_{\mathrm{FS}} \frac{dk g_\perp(\mathbf{k})}{|\nabla_\mathbf{k}\mathcal{E}(\mathbf{k})|}, \tag{2}$$

where the line integral is taken along the zero-field Fermi surface. It is convenient to introduce the transverse g-

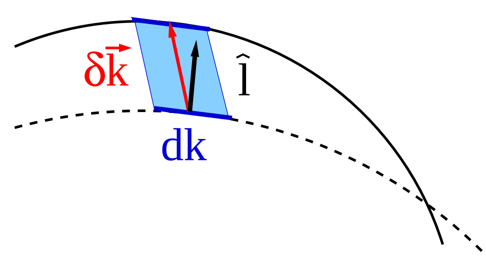

Supplementary Figure 1. Fermi surface of a two-dimensional conductor in zero field (dashed line) and in a transverse field $\mathbf{B}_\perp$ (solid line). Upon turning on $\mathbf{B}_\perp$, a Fermi-surface element dk shifts by a small momentum $\delta\mathbf{k}$ (see the main text), adding the shaded trapezoid of the area $d\mathcal{F} = dk(\delta\mathbf{k}\cdot\hat{\mathbf{l}}_\mathbf{k})$ to the area enclosed by the Fermi surface, where $\hat{\mathbf{l}}_\mathbf{k} = \boldsymbol{\nabla}_\mathbf{k}\mathcal{E}(\mathbf{k})/|\boldsymbol{\nabla}_\mathbf{k}\mathcal{E}(\mathbf{k})|$ is the local unit vector, normal to the Fermi surface. The total variation of the Fermi-surface area is given by integrating $d\mathcal{F}$ over the Fermi surface, as explained in the main text.

* revaz@irsamc.ups-tlse.fr
† t.helm@hzdr.de
‡ TNG Technology Consulting GmbH, 85774 Unterföring, Germany
§ mark.kartsovnik@wmi.badw.de

factor, averaged over the Fermi surface:

$$\bar{g}_\perp = \oint_{\rm FS} \frac{\hbar^2 dk}{2\pi m} \frac{g_\perp(\mathbf{k})}{|\nabla_{\mathbf{k}}\mathcal{E}(\mathbf{k})|}, \tag{3}$$

where

$$m = \frac{1}{2\pi} \oint_{\rm FS} \frac{\hbar^2 dk}{|\nabla_{\mathbf{k}}\mathcal{E}(\mathbf{k})|} \tag{4}$$

is the ($\theta = 0\,°$) cyclotron mass. Substituting $\mu_{\rm B} = \frac{e\hbar}{2m_{\rm e}}$ into Eq. (2), we combine it with Eq. (1) to arrive at the expression for the spin-reduction factor:

$$R_{\rm s}(\theta) = \cos\left[\frac{\pi}{\cos\theta}\frac{\bar{g}_\perp m}{2m_{\rm e}}\right], \tag{5}$$

that is Eq. (2) of the main text. For a momentum-independent $g_\perp$, Eq. (5) matches the textbook expression [1] for the spin-reduction factor in two dimensions.

SUPLEMENTARY NOTE II. SYMMETRY ANALYSIS OF THE NÉEL STATES OF κ-(BETS) AND NCCO

A. Symmetry analysis of the Néel state of κ-(BETS)$_2$FeBr$_4$ in a transverse field

The existence of a special set of momenta in the Brillouin zone (BZ), where Bloch eigenstates of a Néel antiferromagnet remain degenerate in transverse magnetic field, is a general phenomenon. However, the precise geometry of this set depends on the interplay between the periodicity of the Néel order and the symmetry of the underlying crystal lattice [2, 3]. Here, we describe this set for κ-(BETS)$_2$FeBr$_4$, hereafter referred to as κ-BETS.

Upon transition from the paramagnetic to Néel state, the lattice period of κ-BETS along the c axis doubles, and the symmetry of the paramagnetic state with respect to both the time reversal $\hat{\theta}$ and the elementary translation $\hat{\mathbf{T}}_c$ along the c axis is broken. Yet, the product $\hat{\theta}\hat{\mathbf{T}}_c$ remains a symmetry operation, along with the spin rotation $\hat{\mathbf{U}}_{\mathbf{n}}(\phi)$ around the Néel axis $\mathbf{n}$ by an arbitrary angle ϕ.

Applied transversely to $\mathbf{n}$, a magnetic field breaks the symmetry with respect to both $\hat{\theta}\hat{\mathbf{T}}_c$ and $\hat{\mathbf{U}}_{\mathbf{n}}(\phi)$; however, $\hat{\mathbf{U}}_{\mathbf{n}}(\pi)\hat{\theta}\hat{\mathbf{T}}_c$ remains a symmetry operation [2, 3]. It maps a Bloch eigenstate $|\mathbf{k}\rangle$ at wave vector $\mathbf{k}$ onto a degenerate orthogonal eigenstate $\hat{\mathbf{U}}_{\mathbf{n}}(\pi)\hat{\theta}\hat{\mathbf{T}}_c|\mathbf{k}\rangle$ at wave vector $-\mathbf{k}$, as shown in Fig. 2. Upon combination with reflection $\hat{\mathbf{R}}_a$: $(k_c, k_a) \to (k_c, -k_a)$, the resulting symmetry operation $\hat{\mathbf{R}}_a\hat{\mathbf{U}}_{\mathbf{n}}(\pi)\hat{\theta}\hat{\mathbf{T}}_c$ maps $|\mathbf{k}\rangle$ at wave vector $\mathbf{k} = (k_c, k_a)$ onto a degenerate orthogonal eigenstate $\hat{\mathbf{R}}_a\hat{\mathbf{U}}_{\mathbf{n}}(\pi)\hat{\theta}\hat{\mathbf{T}}_c|\mathbf{k}\rangle$ at wave vector $(-k_c, k_a)$ [2, 3].

For an arbitrary $\mathbf{k} = (k_c, k_a)$ at the vertical segment $k_c = \pi/2c$ of the magnetic BZ boundary, the wave vectors $(-k_c, k_a)$ and (k_c, k_a) differ by the reciprocal wave vector $\mathbf{Q} = (\pi/c, 0)$ of the Néel state; in the nomenclature of the magnetic BZ, they are one and the same vector. The degeneracy of such a $|\mathbf{k}\rangle$ with $\hat{\theta}\hat{\mathbf{T}}_c\hat{\mathbf{R}}_a\hat{\mathbf{U}}_{\mathbf{n}}(\pi)|\mathbf{k}\rangle$ means that $g_\perp(\mathbf{k})$ vanishes at the entire segment $k_c = \pi/2c$.

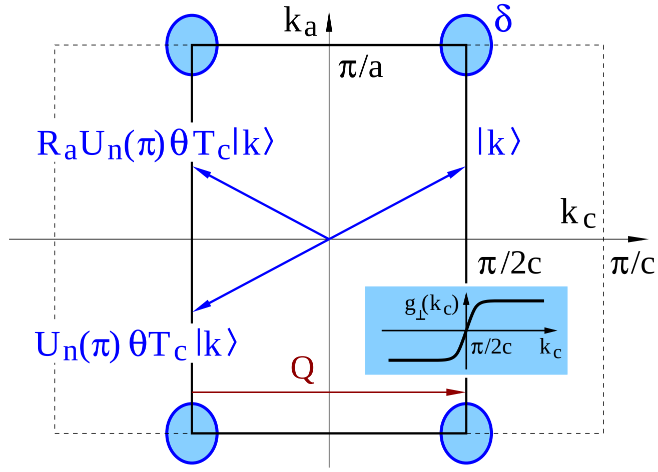

Supplementary Figure 2. **Schematic view of the BZ of κ-BETS.** The BZ in its paramagnetic state (dashed line) and in the Néel state with wave vector $\mathbf{Q} = (\pi/c, 0)$ (solid line). The δ pocket is centered at the corner $\mathbf{k} = (\pm\pi/2c, \pm\pi/a)$ of the magnetic BZ. The arrows show an exact Bloch eigenstate $|\mathbf{k}\rangle$ at a wave vector $\mathbf{k}$ on the vertical segment $k_c = \pi/2c$ of the magnetic BZ boundary – and its symmetry partners $\mathbf{U}_{\mathbf{n}}(\pi)\theta\mathbf{T}_c|\mathbf{k}\rangle$ and $\mathbf{R}_a\mathbf{U}_{\mathbf{n}}(\pi)\theta\mathbf{T}_c|\mathbf{k}\rangle$. The orthogonality $\langle\mathbf{k}|\mathbf{R}_a\mathbf{U}_{\mathbf{n}}(\pi)\theta\mathbf{T}_c|\mathbf{k}\rangle = 0$ implies that $g_\perp(\mathbf{k})$ vanishes on the segment $k_c = \pi/2c$. The inset illustrates the $g_\perp(\mathbf{k})$ being an odd function of $k_c - \pi/2c$.

The δ pocket is centered at $(\pm\pi/2c, \pm\pi/a)$ and is symmetric with respect to reflection around the line $k_c = \pm\pi/2c$, as shown in Figs. 1 and 2. At the same time, as shown in Supplemental Material **SUPLEMENTARY NOTE IV** and illustrated in the insets of Figs. 1 and 2, $g_\perp(\mathbf{k})$ is odd under reflection around the same line. As a result, for the δ pocket $\bar{g}_\perp$ in Eq. (3) vanishes, as stated in the main text.

B. Symmetry analysis of the Néel state of Nd$_{2-x}$Ce$_x$CuO$_4$ in a transverse field

In the antiferromagnetic state of Nd$_{2-x}$Ce$_x$CuO$_4$ (hereafter NCCO), the Cu^{2+} spins point along the layers. At zero field, they form a so-called non-collinear structure: the staggered magnetization vectors of adjacent layers are normal to each other, pointing along the crystallographic directions [100] and [010], respectively (see Ref. [4] for a review). However, an in-plane field above 5 T transforms this spin structure into a collinear one, with the staggered magnetization in all the layers aligned transversely to the field. Therefore, in our experiment, with the field $B > 45$ T rotated around the [100] axis, the staggered magnetization is normal to the field at

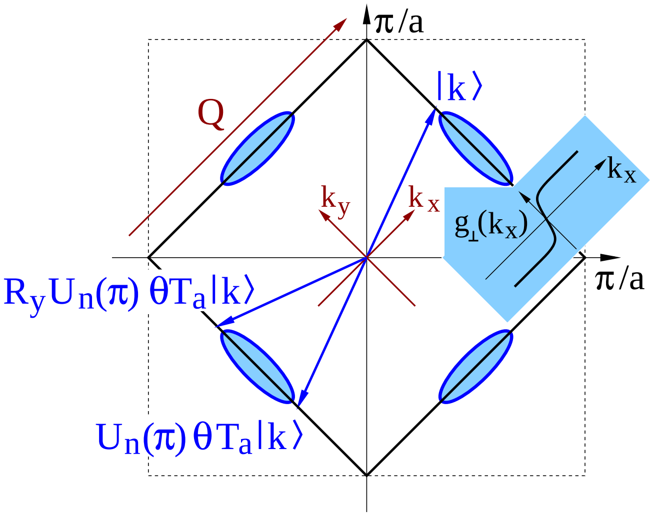

Supplementary Figure 3. **Schematic view of the BZ of NCCO.** The BZ in its paramagnetic state (dashed line) and in the Néel state with wave vector $\mathbf{Q} = (\pi/a, \pi/a)$ (solid line). The carrier pockets α are centered at the midpoints $\mathbf{k} = (\pm\pi/2a, \pm\pi/2a)$ of the magnetic BZ boundary. The blue arrows show an exact Bloch eigenstate $|\mathbf{k}\rangle$ at a wave vector $\mathbf{k}$ on the magnetic BZ boundary – and its symmetry partners $\mathbf{U_n}(\pi)\theta\mathbf{T}_a|\mathbf{k}\rangle$ and $\mathbf{R}_y\mathbf{U_n}(\pi)\theta\mathbf{T}_a|\mathbf{k}\rangle$. The orthogonality $\langle\mathbf{k}|\mathbf{R}_y\mathbf{U_n}(\pi)\theta\mathbf{T}_a|\mathbf{k}\rangle = 0$ implies that $g_\perp(\mathbf{k})$ vanishes on the segment $k_x a = \pm\pi/\sqrt{2}$. The inset illustrates $g_\perp(\mathbf{k})$ being an odd function of $k_x a - \pi/\sqrt{2}$.

all tilt angles except for a narrow interval $0^\circ < |\theta| \lesssim 5^\circ$.

Thus, we can restrict ourselves to the purely transverse-field geometry, with the field normal to the Néel axis, which makes the analysis similar to that for κ-BETS. The only difference is that, given the tetragonal symmetry of NCCO, the triple product $\hat{\mathbf{U}}_\mathbf{n}(\pi)\hat{\theta}\hat{\mathbf{T}}_a$ can now be combined with reflections $\hat{\mathbf{R}}_x$: $(k_x, k_y) \to (-k_x, k_y)$ and $\hat{\mathbf{R}}_y$: $(k_x, k_y) \to (k_x, -k_y)$. As a result, for any wave vector $\mathbf{k}$ at the magnetic Brillouin-zone boundary, one finds $\langle\mathbf{k}|\hat{\mathbf{R}}_y\hat{\mathbf{U}}_\mathbf{n}(\pi)\hat{\theta}\hat{\mathbf{T}}_a|\mathbf{k}\rangle = \langle\mathbf{k}|\hat{\mathbf{R}}_x\hat{\mathbf{U}}_\mathbf{n}(\pi)\hat{\theta}\hat{\mathbf{T}}_a|\mathbf{k}\rangle = 0$. This guarantees double degeneracy of Bloch eigenstates, hence the equality $g_\perp(\mathbf{k}) = 0$ at the entire boundary of the magnetic BZ, as shown in Fig. 3.

The charge-carrier pockets of our interest are believed to be centered at $(\pm\pi/2a, \pm\pi/2a)$, and are symmetric with respect to reflections $\mathbf{R}_x$ and $\mathbf{R}_y$ around the k_x and k_y axes, as shown in Figs. 4 and 3. At the same time, as shown in Section **SUPLEMENTARY NOTE IV** and illustrated in the inset of Figs. 4 and 3, $g_\perp(\mathbf{k})$ is odd under the very same reflections. As a result, $\bar{g}_\perp$ in Eq. (3) vanishes for these pockets, as stated in the main text.

SUPLEMENTARY NOTE III. ESTIMATING THE PRODUCT $k_F\xi$

A. δ pocket in κ-BETS

Looking only for a crude estimate, we assume a parabolic energy dispersion and treat the δ pocket as circular of radius k_F and area $\mathcal{F}_\delta = 2\pi e F_\delta/\hbar$. Defining the antiferromagnetic coherence length as $\xi = \hbar v_F/\Delta_{AF}$, we find:

$$k_F\xi = \hbar k_F v_F/\Delta_{AF} = 2\varepsilon_F/\Delta_{AF}. \tag{6}$$

The Fermi energy ε_F in Eq. (6) can be expressed via the Shubnikov-de Haas (SdH) frequency $F_\delta = 61\,\mathrm{T}$:

$$\varepsilon_F = \frac{\hbar^2 k_F^2}{2m} = \frac{\hbar^2\mathcal{F}_\delta}{2\pi m} = \frac{\hbar e F_\delta}{m} \approx 6\,\mathrm{meV}. \tag{7}$$

Assuming a BSC-like relation between the Néel temperature, $T_N \approx 2.5\,\mathrm{K}$, and the antiferromagnetic gap Δ_{AF} in the electron spectrum, we evaluate the latter as $\Delta_{AF} \simeq 1.8 k_B T_N \approx 0.4\,\mathrm{meV}$. A similar estimate is obtained from the critical field, $B_c \approx 5\,\mathrm{T}$, required to suppress the Néel state: $\Delta_{AF} \sim \mu_B B_c \approx 0.3\,\mathrm{meV}$.

Thus, we find $k_F\xi \simeq \frac{2\varepsilon_F}{\Delta_{AF}} \sim 30 - 40 \gg 1$, which means that $g_\perp(\mathbf{k})$ is nearly constant over most of the Fermi surface, except in a small vicinity of $k_c = \pi/2c$, where it changes sign, cf. Figs. 2 and 4.

B. Small hole pocket of the reconstructed Fermi surface in NCCO

In NCCO, the small Fermi-surface pocket α, responsible for the observed oscillations, is far from being circular. Therefore, we can no longer estimate $k_F\xi$ the same way as we did for the δ pocket in κ-BETS. Instead, we evaluate the relevant Fermi wave vector and the antiferromagnetic coherence length separately.

The value of the Fermi wave vector in the direction normal to the magnetic BZ boundary can be found from ARPES maps of the Fermi surface [5–7]: $k_F = 0.4 \pm 0.1\,\mathrm{nm}^{-1}$.

The coherence length can be estimated using the MB gap value, $\Delta_{AF} \approx 16\,\mathrm{meV}$, and parameters of the (approximately circular) large parent Fermi surface obtained from the analysis of MB quantum oscillations [8]. Using the corresponding SdH frequency $F = 11.25\,\mathrm{kT}$ and cyclotron mass $m = 3.0 m_e$, we estimate the Fermi velocity, $v_F \sim \hbar k_F/m \approx \sqrt{2\hbar e F}/m \approx 2.2 \times 10^5\,\mathrm{m/s}$, which leads to the coherence length $\xi \sim \hbar v_F/\Delta_{AF} \approx 9\,\mathrm{nm}$.

This yields the product $k_F\xi \sim 3 - 5$, which implies $g_\perp(\mathbf{k})$ being piecewise nearly constant over most of the Fermi surface, except in a small vicinity of the magnetic BZ boundary, where $g_\perp(\mathbf{k})$ changes sign, cf. Figs. 3 and 4.

SUPLEMENTARY NOTE IV. SYMMETRY PROPERTIES OF $g_\perp(\mathbf{k})$

In Section **SUPLEMENTARY NOTE II A**, we have shown that in κ-BETS the factor $g_\perp(\mathbf{k})$ vanishes at the entire $k_c = \pm\pi/2c$ segment of the magnetic BZ boundary. Here, we establish an important general symmetry property of $g_\perp(\mathbf{k})$. In the case of κ-BETS, this property implies that $g_\perp(\mathbf{k})$ is an odd function of $k_c - \pi/2c$. The δ pocket, responsible for the observed SdH oscillations, is centered on this segment, at the corner of the magnetic BZ (see Fig. 1). As a result, for this pocket the "effective g-factor" $\bar{g}_\perp$ in Eq. (3) vanishes by symmetry.

Without loss of generality, we consider the simplest case of double commensurability, relevant to both materials of our interest. In both of them, the underlying non-magnetic state is centrosymmetric, with the relevant electron band having the spectrum $\varepsilon(\mathbf{k})$. Spontaneous Néel magnetization with wave vector $\mathbf{Q}$ interacts with the conduction-electron spin $\boldsymbol{\sigma}$ via the exchange term $(\boldsymbol{\Delta}_{\rm AF}\cdot\boldsymbol{\sigma})$, coupling the states at wave vectors $\mathbf{k}$ and $\mathbf{k}+\mathbf{Q}$. In the Néel phase, subjected to magnetic field $\mathbf{B}$, the electron Hamiltonian takes the form [9]

$$\mathcal{H}_{\mathbf{k}} = \begin{bmatrix} \varepsilon(\mathbf{k}) - g\,(\mathbf{B}\cdot\boldsymbol{\sigma}) & (\boldsymbol{\Delta}_{\rm AF}\cdot\boldsymbol{\sigma}) \\ (\boldsymbol{\Delta}_{\rm AF}\cdot\boldsymbol{\sigma}) & \varepsilon(\mathbf{k}+\mathbf{Q}) - g\,(\mathbf{B}\cdot\boldsymbol{\sigma}) \end{bmatrix}, \quad (8)$$

where the factor $\mu_{\rm B}/2$ has been absorbed into the definition of $\mathbf{B}$, and $\boldsymbol{\Delta}_{\rm AF} = J\mathbf{S}$ is the product of the antiferromagnetically ordered moment $\mathbf{S}$ and its exchange coupling J to the conduction electrons. In a purely transverse field $\mathbf{B}_\perp \perp \boldsymbol{\Delta}_{\rm AF}$, the Hamiltonian (8) can be easily diagonalized [2, 10] to yield the spectrum

$$\mathcal{E}(\mathbf{k}) = \varepsilon_+(\mathbf{k}) \pm \sqrt{\Delta_{\rm AF}^2 + [\varepsilon_-(\mathbf{k}) - g\,(\mathbf{B}_\perp\cdot\boldsymbol{\sigma})]^2}, \quad (9)$$

where $\varepsilon_\pm(\mathbf{k}) = \frac{1}{2}\,[\varepsilon(\mathbf{k}) \pm \varepsilon(\mathbf{k}+\mathbf{Q})]$. Equation (9) shows that $\Delta_{\rm AF}$ is the energy gap in the electron spectrum of the Néel state. From Eq. (9), one easily finds the effective transverse g-factor $g_\perp(\mathbf{k})$ [2, 11]

$$g_\perp(\mathbf{k}) = \frac{g\varepsilon_-(\mathbf{k})}{\sqrt{\Delta_{\rm AF}^2 + \varepsilon_-^2(\mathbf{k})}}, \quad (10)$$

plotted in Fig. 4 as a function of momentum component k, normal to the line $g_\perp(\mathbf{k}) = 0$.

The parent paramagnetic state is invariant under time reversal, thus $\varepsilon(\mathbf{k}) = \varepsilon(-\mathbf{k})$. Also, in a doubly-commensurate antiferromagnet with Néel wave vector $\mathbf{Q}$, the wave vector $2\mathbf{Q}$ is a reciprocal lattice vector of the underlying non-magnetic state; thus, $\varepsilon(\mathbf{k}+2\mathbf{Q}) = \varepsilon(\mathbf{k})$. From these properties, it follows that $\mathcal{E}(\mathbf{k}) = \mathcal{E}(-\mathbf{k}+\mathbf{Q})$ and $g_\perp(\mathbf{k}) = -g_\perp(-\mathbf{k}+\mathbf{Q})$ [2]. We will now show how this symmetry property leads to $\bar{g}_\perp = 0$. In NCCO as well as in the Néel state of κ-BETS, the relevant Fermi surface consists of two symmetric parts, which map onto each other under transformation $\mathbf{k} \to -\mathbf{k}+\mathbf{Q}$. Contributions of these two parts to the integral in the right-hand side of Eq. (2) cancel each other exactly; hence, Eq. (3) yields $\bar{g}_\perp = 0$. In other words, Eq. (2) yields $\delta\mathcal{F} = 0$, and thus, in Eqs. (2) and (3) one finds $R_{\rm s}(\theta) = 1$: in a transverse field, the amplitude of magnetic quantum oscillations has no spin zeros.

The arguments above rely on a quasi-classical description. Note that the key conclusion, the absence of spin zeros in a transverse field, holds regardless of how the Fermi wave vector $k_{\rm F}$ compares with the inverse antiferromagnetic coherence length $1/\xi \sim \Delta_{\rm AF}/\hbar v_{\rm F}$, where the behavior of $g_\perp(\mathbf{k})$ crosses over from linear to constant as illustrated in Fig. 4.

In the limit of $k_{\rm F}\xi \lesssim 1$, the problem can be analyzed by reducing the Hamiltonian to the leading terms of its momentum expansion around the band extremum. The conclusion remains intact: in a purely transverse field, the Zeeman term of Eq. (1) does *not* lift the spin degeneracy of Landau levels [12]; hence, the quantum-oscillation amplitude has no spin zeros. The present work extends the validity range of this result from a small Fermi-surface pocket to an arbitrarily large Fermi surface.

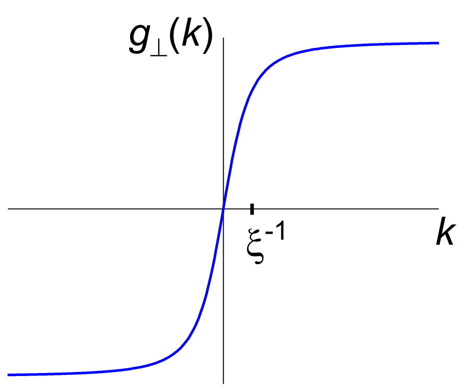

Supplementary Figure 4. **The g-factor for magnetic field normal to the Néel axis.** Schematic plot of $g_\perp(k)$ as a function of the momentum component k, normal to the line $g_\perp(\mathbf{k}) = 0$. At small $k < 1/\xi$, the function $g_\perp(k)$ is linear: $g_\perp(k) \approx g\xi k$. Beyond $k \approx 1/\xi$, $g_\perp(k)$ is nearly constant: $g_\perp(k) \approx g$. Here, $\xi = \hbar v_{\rm F}/\Delta_{\rm AF}$ is the antiferromagnetic coherence length, and $\Delta_{\rm AF}$ is the energy gap in the electron spectrum (9) of the Néel state.

SUPLEMENTARY NOTE V. QUANTUM OSCILLATIONS IN $CeIn_3$

As we pointed out in the main text, for certain Fermi surfaces Zeeman spin-orbit coupling may not manifest itself in quantum oscillations: this is sensitive to where the Fermi surface is centered. An illustrative example is provided by $CeIn_3$, a heavy-fermion compound

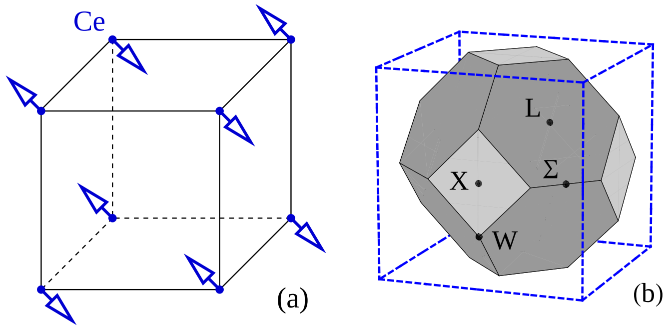

Supplementary Figure 5. Geometry of $CeIn_3$ in real and reciprocal space. (Reprinted from Ref. [2], with permission. © 2009 American Physical Society) (a) Cubic unit cell of $CeIn_3$ in its Néel state, showing Ce atoms and their magnetic moments [13]. Indium atoms (not shown) are located at the face centers of the unit cell. (b) Cubic BZ of paramagnetic $CeIn_3$ shown by dashed lines and, inside, the magnetic BZ. Hexagonal faces (dark gray) form the reciprocal-space surface of the symmetry-protected degeneracy $g_\perp(\mathbf{k}) = 0$.

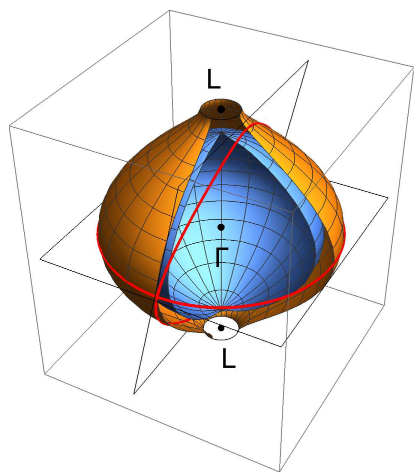

Supplementary Figure 6. Schematic view of the *d* sheet of $CeIn_3$ in the Néel state. We only show a single pair of necks for clarity. The outer sheet illustrates the Fermi-surface reconstruction with broadened necks, the inner sheet shows a reconstruction with the necks truncated. The red lines represent two cyclotron trajectories: a smaller cyclotron-mass trajectory in a magnetic field pointing along ΓL, and a larger cyclotron-mass trajectory, approaching the neck of the Fermi surface.

of simple-cubic Cu_3Au structure, with a moderately enhanced Sommerfeld coefficient, $\gamma = 130\,\mathrm{mJ/K^2\,mol}$. Below $T_\mathrm{N} \approx 10\,\mathrm{K}$, it develops a type-II antiferromagnetic structure with wave vector $\mathbf{Q} = (\frac{\pi}{a}, \frac{\pi}{a}, \frac{\pi}{a})$ and an ordered moment of about $(0.65 \pm 0.1)\,\mu_\mathrm{B}$ per Ce atom [13], shown in Fig. 5(a). The material remains a metallic down to the lowest temperatures. The BZs in the paramagnetic and in the Néel state are shown in Fig. 5(b). In a transverse magnetic field, anti-unitary symmetry protects double degeneracy (and thus the equality $g_\perp(\mathbf{k}) = 0$) on hexagonal faces of the magnetic BZ in Fig. 5(b) [2].

We will focus on the *d* branch of the Fermi surface of $CeIn_3$, a nearly spherical sheet centered at the zone center Γ, with a radius close to $\frac{\sqrt{3}}{2}\frac{\pi}{a}$, where a is the lattice constant. In the paramagnetic state, this sheet has necks protruding out near the L points in Fig. 5(b), connecting it to another sheet centered at the corner of the paramagnetic BZ [14, 15].

The *d* sheet has been studied in detail by quantum oscillations, which revealed a large enhancement of the cyclotron mass upon tilting the field, from $m \approx 2m_0$ for cyclotron trajectories passing far from the necks (e.g., for magnetic field $\mathbf{B}\|\langle 100\rangle$) to $m > 12m_0$ for trajectories approaching the necks (such as $\mathbf{B}\|\langle 110\rangle$) [16, 17]. This mass enhancement can be explained [18] by the Fermi-surface geometry, illustrated in Fig. 6: approaching a neck, the cyclotron trajectory inevitably runs into a saddle point with its concomitant logarithmic enhancement of the cyclotron mass.

Upon transition to the Néel state, the Fermi surface undergoes a reconstruction by folding into the magnetic BZ. Depending on the neck size and on the value of the Néel gap in the electron spectrum, the reconstructed sheets may have their necks broadened or truncated altogether [18], as shown in Fig. 6.

The cyclotron-mass enhancement for those field orientations, for which the quasiclassical trajectories approach a neck [16, 17] is consistent with the Fermi sheet having necks in the Néel state. So is the observation of spin zeros [16]: the enhancement of m/m_0 alone produces spin zeros as the cyclotron trajectory approaches a neck with tilting the field. Crucially for the Zeeman effect that we are interested in, the average of $g_\perp(\mathbf{k})$ over a cyclotron trajectory on the *d* sheet does *not* vanish – simply because most (if not all) of the cyclotron trajectory in question lies *within* the first magnetic BZ, and thus $g_\perp(\mathbf{k})$ keeps its sign over most (or all) of the trajectory. Indeed, being centered at the Γ point, the *d* sheet cannot possibly be symmetric with respect to the surface $g_\perp(\mathbf{k}) = 0$ in Fig. 5(b), and thus our symmetry argument for the vanishing $\bar{g}_\perp$ inevitably breaks down. The observation of spin zeros [16] in $CeIn_3$ is thus perfectly consistent with the physics of the Zeeman spin-orbit coupling described in the main text.

SUPLEMENTARY NOTE VI. SdH OSCILLATIONS IN THE HIGH-FIELD PARAMAGNETIC STATE OF κ-BETS

The SdH oscillations in the high-field, paramagnetic (PM) state of κ-BETS have been described in detail in a number of publications [19–23], revealing a Fermi surface largely consistent with that obtained from band-structure calculations [24]. Here, we give a brief overview, referring to our own data, which show perfect agreement with the previous reports. The measurements were performed on the same crystal as discussed in the main text.

Figure 1(b) in the main text shows an example of the low-temperature interlayer resistance measured in a magnetic field up to 14 T, directed nearly perpendicularly to the conducting layers. The kink around $B_c \approx 5.2$ T reflects the transition from the low-field AF to the high-field PM state. The slow SdH oscillations associated with the small pocket δ (shown in Fig. 1c) of the reconstructed FS in the AF state collapse at B_c. In the PM state, the oscillation spectrum is composed of two fundamental frequencies $F_\alpha \approx 840$ T and $F_\beta \approx 4200$ T and their combinations, as shown in the inset in Fig.1(b). The dominant contribution comes from the α oscillations associated with the closed portion of the Fermi surface centered on the BZ boundary shown in Fig. 1(a). The β oscillations, which are considerably weaker than the α oscillations, originate from the large magnetic-breakdown (MB) orbit enveloping the whole Fermi surface [dashed orange line in Fig. 1(b)]. Additionally, there are sizable contributions of the second harmonic of the α oscillations and combination frequencies, $\beta - p\alpha$ with $p = 1, 2$, in the SdH spectrum, which are often observed in clean, highly two-dimensional organic metals in the intermediate MB regime [25]. The oscillation amplitude shows spin-zeros not only in the angular dependence but also with changing the field strength at a fixed orientation. This is due to the presence of an exchange field B_J imposed on the conduction electrons by saturated paramagnetic Fe^{3+} ions, although some details of its behavior are still to be understood [1, 23, 26]. The analysis of the spin-zero positions in the PM state yields the g-factor very close to that of free electrons, $g = 2.0 \pm 0.2$ and the exchange field $B_J \approx -13$ T pointing against the external magnetic field [23].

Note that both α and β oscillations are rapidly suppressed with lowering the field and cannot be resolved near the transition field B_c. This rapid suppression is due to the relatively high cyclotron masses: compared to the δ-oscillation mass, the α and β masses are some 5 and 7 times higher, respectively. The exponential dependence of the SdH amplitude on the cyclotron mass, see Eq. (3) of the main text, renders the amplitude factor for the α oscillations approximately 2 orders of magnitude smaller than that for the slow δ oscillations at fields near B_c. In addition to the higher cyclotron mass, the MB gap Δ_0 contributes to the damping of the β oscillations via the MB damping factor. This is why the β oscillations are only seen at highest fields, ≥ 10 T, as weak distortions of the α-oscillation wave form and as a small peak in the FFT spectrum.

SUPLEMENTARY NOTE VII. DETAILS OF THE SdH FIT FOR κ-BETS IN THE AF STATE

In the main text, we noted a large uncertainty of B_0 and B_{AF}. Here, we show that the quality of our SdH amplitude fits is insensitive to the exact values of B_0 and B_{AF}. Equation (3) for the amplitude A_δ contains the

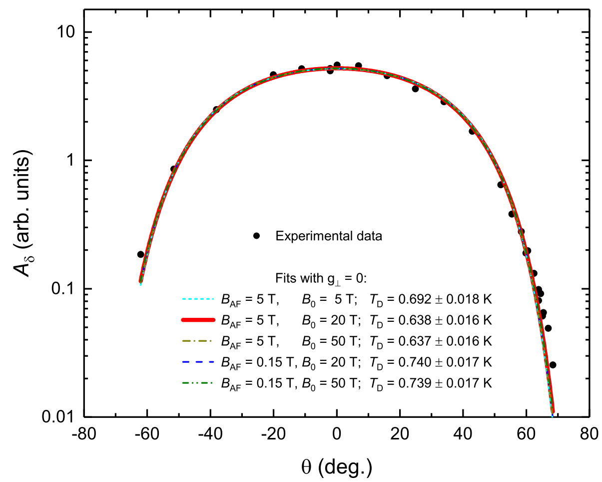

Supplementary Figure 7. Angle-dependent δ oscillation amplitude in κ-BETS compared to theoretical fits. Black dots are the experimental data and lines are fits using Eq. (3) of the main text with different fixed values of the MB fields B_0 and B_{AF}. The angle-independent Dingle temperature T_D and amplitude prefactor A_0 are the fitting parameters and $g_\perp$ is set to zero. The plot demonstrates insensitivity of the angular dependence on the concrete choice of B_0 and B_{AF}.

MB factor

$$R_{MB}^{[\delta]} = \left[1 - \exp\left(-\frac{B_0}{B\cos\theta}\right)\right]\left[1 - \exp\left(-\frac{B_{AF}}{B\cos\theta}\right)\right], \quad (11)$$

which must be taken into account when analyzing the angular dependence $A_\delta(\theta)$.

A rough estimate of B_0 can be obtained from the ratio between the α- and β-oscillation amplitudes at a certain field and temperature, using the LK formula [Eq. (3) of the main text] with the MB factors $R_{MB}^{[\alpha]} = [1 - \exp(-B_0/B)]$ and $R_{MB}^{[\beta]} = \exp(-2B_0/B)$ for the α and β oscillations, respectively. From the data in Fig. 1(b) we estimate the ratio between the FFT amplitudes of the α and β oscillations in the field interval 10 to 14 T, at $T = 0.5$ K, as $A_\beta/A_\alpha \approx 0.03$. To complete the estimation, we also need to know the cyclotron masses, which have been determined in earlier experiments: $m_\alpha = 5.2m_0$ and $m_\beta = 7.9m_0$ [20], and the Dingle temperature T_D. The latter arises from scattering on crystal imperfections [1] and, therefore, varies from sample to sample. As shown below, for the present crystal a reasonable estimate of the Dingle temperature in the AF state, $T_D \simeq 0.7$ K, can be obtained from the angular dependence of the δ-oscillation amplitude. Assuming that T_D is momentum-independent and remains the same in the PM state, we substitute this value in the LK formula, arriving at the MB field value $B_0 \approx 12$ T. This is three times higher than the upper end of the field interval used for the SdH oscillation analysis in the AF state. Therefore, the first factor in the right-hand side of Eq. (11)

is close to unity and does not contribute significantly to the angular dependence $A_\delta(\theta)$. To confirm this, we have checked how our fits are affected by varying B_0 in the range between 5 T and 50 T, as will be presented below. Note: One may expect that T_D in the PM state is somewhat lower than the value $T_\mathrm{D} \approx 0.7\,\mathrm{K}$ obtained for the AF state, due to the absence of scattering on defects of the AF order (e.g., domain walls). If so, the actual MB field is even higher than 12 T, hence the corresponding MB factor is even closer to unity.

The MB field B_AF is due to magnetic ordering and can be estimated from the gap Δ_AF with the help of the Blount criterion [1, 27],

$$B_\mathrm{AF} \sim \frac{m}{\hbar e} \cdot \Delta_\mathrm{AF}^2/\varepsilon_\mathrm{F} \simeq 0.15\,\mathrm{T}\,. \qquad (12)$$

Here, we estimated the Fermi energy ε_F from SdH oscillations in the paramagnetic state: $\varepsilon_\mathrm{F} \sim \hbar^2 k_\mathrm{F}^2/2m \sim \hbar e F_\beta/m_\beta$, with the SdH frequency $F_\beta = 4280$ T and corresponding cyclotron mass $m_\beta = 7.9 m_0$ [20].

Of course, these are only rough estimates. Moreover, the observation of the δ oscillations in fields up to $B_\mathrm{c} \simeq 5\,\mathrm{T}$ implies that the relevant MB field must be in the range of a few tesla, to provide a non-vanishing second factor in the right-hand side of Eq. (11). On the other hand, the MB field cannot be much higher than the fields we applied ($B \lesssim B_\mathrm{c}$). We have tentatively set the upper estimate for B_AF to about 5 T and checked how our fits are affected by varying B_AF from 0.15 T to 5 T.

The results are summarized in Fig. 7, which presents several fits to the experimental data for κ-BETS (the same as in Fig. 3 of the main text), with values of B_0 and B_AF varying in a broad range: $5\,\mathrm{T} \leq B_0 \leq 50\,\mathrm{T}$ and $0.15\,\mathrm{T} \leq B_\mathrm{AF} \leq 5\,\mathrm{T}$. All the fits assume $g_\perp = 0$; as shown in the main text, a finite value for $g_\perp$ would simply lead to sharp spin zeros, insensitive to the monotonic θ dependence of R_MB. One can clearly see that the fits are nearly indistinguishable and virtually insensitive to variation of B_0 within the given range, whereas the variation of B_AF barely results in a 15% change of the Dingle temperature: $T_\mathrm{D} = (0.69 \pm 0.05)\,\mathrm{K}$. The parameter A_0 in Eq. (3) changes roughly in inverse proportion to B_AF. However, A_0 is largely an empirical parameter, irrelevant to our study. Thus, we conclude that the mentioned uncertainty of the MB fields has no effect on the quality of our fits, as stated in the main text.

SUPLEMENTARY NOTE VIII. AMPLITUDE ANALYSIS FOR NCCO

In our experiment on NCCO we were restricted to a relatively narrow field interval, between 45 and 64 T where the oscillations were observable over the whole angular range. Due to the low frequency, this interval contains only a few oscillation periods, see Fig. 8 and Fig. 4 in the main text. Under these conditions the FFT spectrum is sensitive to the choice of the field window and details of the background subtraction. The choice of the upper bound of the field window is most important here: this affects the largest-amplitude oscillation and thus gives the dominant contribution to the overall error. In the course of our analysis we always ensured that the order of the polynomial fit (≤ 4) to the non-oscillating B-dependent background did not affect the height of the FFT peak corresponding to the SdH oscillations, within our resolution. The main source of error is the variation of the oscillation phase at the (fixed) upper end of the field window caused by the changing frequency $F(\theta)$: this disturbs the shape and amplitude of the largest oscillation. In order to reduce this parasitic effect, we kept the FFT window more narrow than that of the background fit; the upper B border of the FFT window was at least 1 T lower than that of the background fit. In our analysis we found that the associated error bar for the height of the FFT peak did not exceed $\pm 10\,\%$. While this uncertainty may be important, for example, for an exact evaluation of the effective cyclotron mass, in our case, when the oscillation amplitude is expected to change an order of magnitude near a spin-zero, it is not significant. Only at highest angles, the error becomes comparable to the signal, which is related to the low signal-to-noise ratio at these conditions.

To crosscheck our FFT analysis we present an alternative amplitude analysis in Fig. 8. For each $R_\mathrm{osc}/R_\mathrm{backg}$ curve, we determine the peak-to-peak amplitude from the linearly interpolated envelopes (dashed black lines in Fig. 8a,b) at a fixed field value. We chose the middle of the FFT window in $1/B$ scale, i.e., $B = [(1/45 + 1/64)/2]^{-1}$ T= 52.8 T, as well as the values 55 T and 60 T, with oscillations discernible up to 67°. Fig. 8c presents these points plotted versus the tilt angle θ and compares them to the FFT values and LK fit from Fig. 3 shown in the main text. The extracted data from both approaches match very well. Clearly, our main conclusion holds, that is, the overall angular dependence exhibits no indication of a spin-zero effect for angles of up to at least 70°.

SUPLEMENTARY NOTE IX. ESTIMATING THE DISPARITY OF SPIN-UP AND SPIN-DOWN TUNNELING AMPLITUDES IN NCCO

The Nd^{3+} spins in the insulating layers of NCCO are polarized by strong magnetic field. Consequently one may wonder whether this spin polarization could render interlayer tunneling amplitudes for spin-up and spin-down different enough to lose spin zeros in the c-axis magnetoresistance oscillations. In the following we will show that this possibility can be ruled out. The ratio of interlayer the conductivities $\sigma_\uparrow$ and $\sigma_\downarrow$ can be crudely estimated via the tunneling amplitudes $w_\uparrow$ and $w_\downarrow$ as

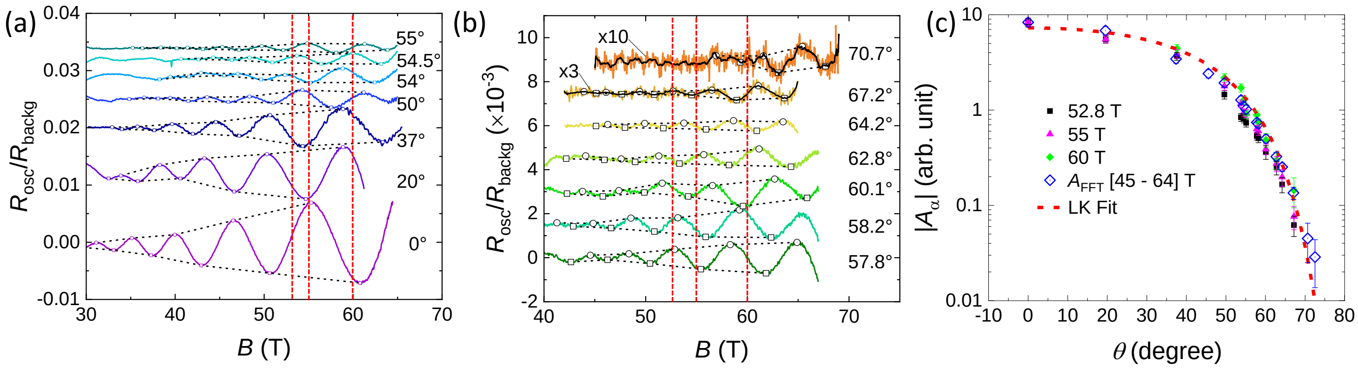

Supplementary Figure 8. Amplitude analysis of the angle-dependent α oscillations in NCCO. (a) and (b) oscillating resistance component, normalized to the non-oscillating B-dependent background, plotted as a function of magnetic field. The curves corresponding to different tilt angles θ are vertically shifted for clarity. For $\theta = 67.2^\circ$ and 70.7° the ratio $R_{\mathrm{osc}}/R_{\mathrm{backg}}$ is multiplied by a factor of 3 and 10, respectively. The vertical dashed lines indicate the field values at which we determine $A(\theta)$ shown in (c). (c) Normalized peak-to-peak oscillation amplitude determined for $B = 52.8\,\mathrm{T}$, $55\,\mathrm{T}$, and $60\,\mathrm{T}$ in comparison to the amplitude determined by FFT for $B = [45 - 64]\,\mathrm{T}$. Red dashed line is the fit with $g = 0$, see Fig. 5 in the main text.

$$\frac{\sigma_\uparrow}{\sigma_\downarrow} \approx \frac{w_\uparrow^2}{w_\downarrow^2} = \exp\left(-\frac{2}{\hbar}\int dz\left[\sqrt{2m\left(U\left(z\right)-E_{\mathrm{F}}-E_{\mathrm{Z}}/2\right)}-\sqrt{2m\left(U\left(z\right)-E_{\mathrm{F}}+E_{\mathrm{Z}}/2\right)}\right]\right),$$

where $U(z)$ is the tunneling potential and E_{Z} the Zeeman splitting, responsible for the difference between $\sigma_\uparrow$ and $\sigma_\downarrow$. For a rough estimate, it suffices to replace $U(z)$ by a rectangular potential barrier of spatial width d, the unperturbed tunneling amplitude being $w = \exp\left(-d\sqrt{2m\left(U\left(z\right)-E_{\mathrm{F}}\right)}/\hbar\right)$. The expression in the exponent above can then be expanded in small E_{Z} to yield

$$\frac{\sigma_\uparrow}{\sigma_\downarrow} \approx \exp\left(\frac{E_{\mathrm{Z}}}{U-E_{\mathrm{F}}}\frac{\sqrt{2m\left(U-E_{\mathrm{F}}\right)}d}{\hbar}\right) = \exp\left[-\frac{E_{\mathrm{Z}}}{U-E_{\mathrm{F}}}\ln w\right].$$

To put in the numbers, notice that the deviation of the experimental data in Fig. 5 of the main text from the theoretical fit with $R_{\mathrm{s}} = 1$ does not exceed 20%. Assuming this deviation to be entirely due to an interference of unequal spin-up and spin-down oscillation amplitudes would imply $\sigma_\uparrow/\sigma_\downarrow \sim 20$. Let us estimate the E_{Z} required for such a behavior. Recall that w is essentially the ratio of a typical interlayer hopping amplitude $t_z \sim 10^{-2}$ eV to the in-plane Fermi scale $U - E_{\mathrm{F}} \sim 1$ eV, and thus $\ln w \approx -4.6$. The ratio $\sigma_\uparrow/\sigma_\downarrow \sim 20$ would then mean $E_{\mathrm{Z}} \gtrsim 0.6$ eV: an unrealistic bound, which allows us to rule out this scenario.

SUPPLEMENTARY REFERENCES

[1] Shoenberg, D. *Magnetic Oscillations in Metals* (Cambridge University Press, Cambridge, 1984).
[2] Ramazashvili,R. *Kramers degeneracy in a magnetic field and Zeeman spin-orbit coupling in antiferromagnetic conductors*, Phys. Rev. B **79,** 184432 (2009).
[3] Ramazashvili, R. *Kramers degeneracy in a magnetic field and Zeeman spin-orbit coupling in antiferromagnetic conductors.* Phys. Rev. Lett. **101,** 137202 (2008).
[4] Armitage, N. P., Fournier, P. & Greene, R. L. *Progress and perspectives on electron-doped cuprates.* Rev. Mod. Phys. **82,** 2421-2487 (2010).
[5] He, J.-F. *et al. Fermi surface reconstruction in electron-*

doped cuprates without antiferromagnetic long-range order. Proc. Natl. Acad. Sci. USA **116,** 3449-3453 (2019).

[6] Armitage, N. P. *et al. Doping dependence of an n-type cuprate superconductor investigated by angle-resolved photoemission spectroscopy.* Phys. Rev. Lett. **88,** 257001 (2002).

[7] Matsui, H. *et al. Evolution of the pseudogap across the magnet-superconductor phase boundary of* $Nd_{2-x}Ce_xCuO_4$, Phys. Rev. B **75,** 224514 (2007).

[8] Helm, T. *et al. Correlation between Fermi surface transformations and superconductivity in the electron-doped high-*T_c *superconductor* $Nd_{2-x}Ce_xCuO_4$. Phys. Rev. B **92,** 094501 (2015).

[9] Kulikov, N. I. & Tugushev, V. V. *Spin density waves and band antiferromagnetism in metals.* Usp. Fiz. Nauk **144,** 643 (1984) [Sov. Phys. Usp. **27,** 954-976 (1984)].

[10] Brazovskii, S. A. Luk'yanchuk, I. A. & Ramazashvili, R. R. *Electron paramagnetism in antiferromagnets.* JETP Lett. **49,** 644-646 (1989).

[11] Kabanov, V.V. & Alexandrov, A. S. *Magnetic quantum oscillations in doped antiferromagnetic insulators.* Phys. Rev. B **77,** 132403 (2008); **81,** 099907(E) (2010).

[12] Ramazashvili, R. *Electric excitation of spin resonance in antiferromagnetic conductors.* Phys. Rev. B **80,** 054405 (2009).

[13] Lawrence, J. M. & Shapiro, S. M. *Magnetic ordering in the presence of fast spin fluctuations: A neutron scattering study of* $CeIn_3$. Phys. Rev. B **22,** 4379-4388 (1980).

[14] Biasini, M. Ferro, G. & Czopnik, A. *Fermi-surface topology of the heavy-fermion antiferromagnetic superconductor* $CeIn_3$. Phys. Rev. B **68,** 094513 (2003).

[15] Rusz, J. & Biasini, M. *Nature of f-electrons in* $CeIn_3$*: Theoretical analysis of positron annihilation data.* Phys. Rev. B **71,** 233103 (2005).

[16] Settai, R. *et al. De Haas – van Alphen studies of rare earth compounds.* J. Magn. Magn. Mater. **140–144,** 1153-1154 (1995).

[17] Ebihara, T., Harrison, N., Jaime, M., Uji, S. & Lashley, J. C. *Emergent fluctuation hot spots on the Fermi surface of* $CeIn_3$ *in strong magnetic fields.* Phys. Rev. Lett. **93,** 246401 (2004).

[18] Gor'kov, L. P. & Grigoriev, P. D. *Antiferromagnetism and hot spots in* $CeIn_3$. Phys. Rev. B **73,** 060401(R) (2006).

[19] Balicas, L. *et al. Shubnikov–de Haas effect and Yamaji oscillations in the antiferromagnetically ordered organic superconductor* κ-$(BETS)_2FeBr_4$*: a fermiology study.* Solid State Commun. **1**16, 557-562 (2000).

[20] Uji, S. *et al. Two-dimensional Fermi surface for the organic conductor* κ-$(BETS)_2FeBr_4$. Physica B **298,** 557-561 (2001).

[21] Konoike, T. *et al. Fermi surface reconstruction in the magnetic-field-induced superconductor* κ-$(BETS)_2FeBr_4$. Phys. Rev. B **72,** 094517 (2005).

[22] Konoike, T. *et al. Anomalous magnetic-field-hysteresis of quantum oscillations in* κ-$(BETS)_2FeBr_4$. J. Low Temp. Phys. **142,** 531-534 (2006).

[23] Kartsovnik, M. V. *et al. Interplay between conducting and magnetic systems in the antiferromagnetic organic superconductor* κ-$(BETS)_2FeBr_4$. J. Supercond. Nov. Magn. **29,** 3075-3080 (2016).

[24] Fujiwara, H. *et al. A novel antiferromagnetic organic superconductor* κ-$(BETS)_2FeBr_4$ *[where BETS = Bis(ethylenedithio)tetraselenafulvalene].* J. Am. Chem. Soc. **123,** 306-314 (2001).

[25] Kartsovnik, M. V. *High magnetic fields: A tool for studying electronic properties of layered organic metals.* Chem. Rev. **104,** 5737-5782 (2004).

[26] Cépas, O., McKenzie, R. H. & Merino, J. *Magnetic-field-induced superconductivity in layered organic molecular crystals with localized magnetic moments.* Phys. Rev. B **65,** 100502(R) (2002).

[27] Blount, E. I. *Bloch electrons in a magnetic field.* Phys. Rev. **126,** 1636-1653 (1962).